

10 GaN-based Light-Emitting Diodes

J. Piprek¹ and S. Li²

¹ University of California, Santa Barbara, CA 93106-9560, U.S.A.,
piprek@ieee.org

² Crosslight Software, 202-3855 Henning Dr., Burnaby, BC V5C 6N3 Canada,
simon@crosslight.com

10.1 Introduction

Light-emitting diodes (LEDs) offer several advantages over traditional light sources, such as smaller size, longer lifetime, higher efficiency, and greater mechanical ruggedness. Continuing developments in LED technology are producing devices with increased output power and efficiency as well as a wider range of colors [1]. Recent progress in the fabrication of GaN-based compound semiconductors enabled the practical breakthrough of short-wavelength LEDs that emit green, blue, or ultraviolet light [2]. In particular, compact ultraviolet (UV) light sources are currently of high interest for applications in white-light generation, short-range communication, water purification, and biochemical detection. Prime candidates are nitride LEDs with AlGaN quantum wells. However, their performance is still below the requirement for practical applications.

We present here a self-consistent physics-based three-dimensional (3D) simulation of an AlGaN/GaN LED and study performance limiting internal mechanisms. Good agreement with measured device characteristics [3] is achieved by refinement of the physical model and by calibration of material parameters. Based on this agreement, we are able to analyze the practical impact of microscale and nanoscale physical effects such as current crowding, carrier leakage, nonradiative recombination, and built-in polarization.

The device structure is given in the next section. Section 10.3 describes the theoretical models and the material parameters used. The main simulation results are presented and discussed in Sect. 10.4.

10.2 Device Structure

Our example device was grown on *c*-face sapphire by metal organic chemical vapor deposition (MOCVD) [3]. The layer structure is given in Table 10.1. It includes an AlGaN multi-quantum well (MQW) active region that is covered by a p -Al_{0.3}Ga_{0.7}N electron blocker layer. MQW and blocker layer are sandwiched between two 42-period AlGaN superlattice (SL) cladding layers. A quadratic mesa with 300- μ m edge length is etched down to the *n*-GaN contact layer. The U-shaped *n*-side contact covers three of the four sides of the

mesa (Fig. 10.1). The top p -contact layer is semi-transparent for top emission. More details on device design, fabrication, and performance are given in [3, 4].

Table 10.1. Layer Structure and Room-Temperature Parameters of the Al-GaN/GaN LED (d , layer thickness; N_{dop} , doped carrier density; μ , majority carrier mobility (low field); n_r , refractive index at wavelength 340 nm; κ_L , lattice thermal conductivity).

Parameter	d Unit (nm)	N_{dop} ($1/\text{cm}^3$)	μ (cm^2/Vs)	n_r —	κ_L (W/cmK)
p -GaN	5	1×10^{18}	10	2.77	1.3
p -AlGaIn SL cladding	126	4×10^{17}	0.5	2.48	0.2
p -Al _{0.3} Ga _{0.7} In blocker	15	1×10^{17}	5	2.02	0.1
i -Al _{0.10} Ga _{0.90} N well	5	—	300	2.79	0.2
n -Al _{0.16} Ga _{0.84} N barrier	13	2×10^{18}	185	2.48	0.2
i -Al _{0.10} Ga _{0.90} N well	5	—	300	2.79	0.2
n -Al _{0.16} Ga _{0.84} N barrier	13	2×10^{18}	185	2.48	0.2
i -Al _{0.10} Ga _{0.90} N well	5	—	300	2.79	0.2
n -Al _{0.16} Ga _{0.84} N barrier	13	2×10^{18}	185	2.48	0.2
i -Al _{0.10} Ga _{0.90} N well	5	—	300	2.79	0.2
n -AlGaIn SL cladding	126	2×10^{18}	10	2.48	0.2
n -GaN contact layer	500	2×10^{18}	200	2.77	1.3

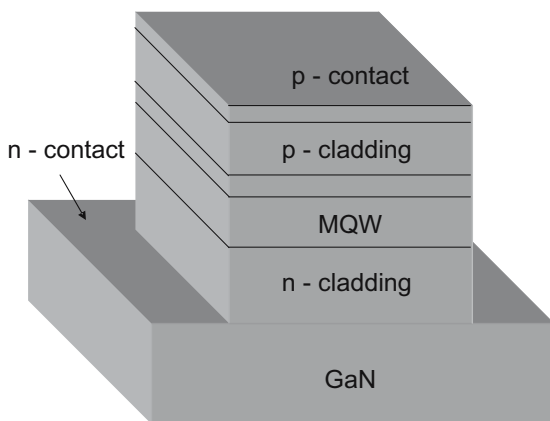


Fig. 10.1. Schematic 3D view of the light-emitting diode structure.

10.3 Models and Parameters

We employ the simulation software APSYS [5], which self-consistently combines the 3D simulation of carrier transport, self-heating, spontaneous photon emission, and optical ray tracing. The code was significantly improved during our investigation to provide more realistic results. The wurtzite energy band structure is considered for all GaN-based semiconductors. The main features of the models are summarized in the following, and more details can be found in [6].

The inclusion of correct material parameters is of paramount importance for realistic device simulations. These parameters depend on the material composition and may be different for every layer in the device. Published values sometimes spread over a wide range, and it is difficult to select the number most appropriate for a given device. We therefore include a detailed discussion of those material parameters that are crucial for our simulation. Hereby, we mainly rely on the recent review of III-nitride parameters in [7]. Binary material parameters are listed in Table 10.2, and they are interpolated linearly for AlGa_N unless noted otherwise in the following.

10.3.1 Wurtzite Energy Band Structure

Most GaN-based semiconductor compounds are grown as wurtzite (hexagonal) crystals. Their energy band structure is different from that of traditional zinc blende III-V semiconductors. The three valence bands of wurtzite semiconductors are referred to as heavy-hole (hh), light-hole (lh), and crystal-field split-hole (ch) band. Spin-orbit interaction leads to only slight separations between the three band edges. We here briefly summarize the 6×6 $\mathbf{k} \cdot \mathbf{p}$ model for the band structure of strained wurtzite semiconductors as developed by Chuang and Chang [8, 9]. Their material parameters are replaced by the more recent data listed in Table 10.2.

The epitaxial growth of Al_xGa_{1-x}N on GaN is typically along the c axis of the wurtzite crystal, which is parallel to the z axis in our coordinate system. The natural lattice constant $a_0(x)$ is enlarged to the one of the GaN substrate, a_s , imposing biaxial tensile strain in the transverse plane

$$\epsilon_t = \frac{a_s - a_0}{a_0} \quad (10.1)$$

and compressive strain in the growth direction

$$\epsilon_z = -2 \frac{C_{13}}{C_{33}} \epsilon_t. \quad (10.2)$$

The nondiagonal elements of the strain tensor are zero. The valence band edge energies are

Table 10.2. Material Parameters used for Wurtzite Semiconductors GaN and AlN at Room Temperature [7] ($\Delta_{\text{cr}} = \Delta_1$, $\Delta_{\text{so}} = 3\Delta_2 = 3\Delta_3$).

Parameter	Symbol	Unit	GaN	AlN
Electron eff. mass (<i>c</i> axis)	m_c^z	m_0	0.20	0.32
Electron eff. mass (transverse)	m_c^t	m_0	0.20	0.30
Hole eff. mass parameter	A_1	—	-7.21	-3.86
Hole eff. mass parameter	A_2	—	-0.44	-0.25
Hole eff. mass parameter	A_3	—	6.68	3.58
Hole eff. mass parameter	A_4	—	-3.46	-1.32
Hole eff. mass parameter	A_5	—	-3.40	-1.47
Hole eff. mass parameter	A_6	—	-4.90	-2.64
Direct band gap (unstrained)	E_g^0	eV	3.438	6.158
Thermal band gap shrinkage	dE_g^0/dT	meV/K	-0.42	-0.56
Spin-orbit split energy	Δ_{so}	eV	0.017	0.019
Crystal-field split energy	Δ_{cr}	eV	0.01	-0.169
Lattice constant	a_0	Å	3.189	3.112
Elastic constant	C_{33}	GPa	398	373
Elastic constant	C_{13}	GPa	106	108
Hydrost. deform. potential (<i>c</i> axis)	a_z	eV	-4.9	-3.4
Hydrost. deform. potential (transverse)	a_t	eV	-11.3	-11.8
Hydrost. deform. potential (cond. band)	a_c	eV	-6.8	-7.6
Shear deform. potential	D_1	eV	-3.7	-17.1
Shear deform. potential	D_2	eV	4.5	7.9
Shear deform. potential	D_3	eV	8.2	8.8
Shear deform. potential	D_4	eV	-4.1	-3.9
dielectric constant	ε	—	9.5	8.5

$$E_{\text{hh}} = E_{\text{v}} + \Delta_1 + \Delta_2 + \theta_{\epsilon} + \lambda_{\epsilon} \quad (10.3)$$

$$E_{\text{lh}} = E_{\text{v}} + \frac{\Delta_1 - \Delta_2 + \theta_{\epsilon}}{2} + \lambda_{\epsilon} + \sqrt{\left(\frac{\Delta_1 - \Delta_2 + \theta_{\epsilon}}{2}\right)^2 + 2\Delta_3^2} \quad (10.4)$$

$$E_{\text{ch}} = E_{\text{v}} + \frac{\Delta_1 - \Delta_2 + \theta_{\epsilon}}{2} + \lambda_{\epsilon} - \sqrt{\left(\frac{\Delta_1 - \Delta_2 + \theta_{\epsilon}}{2}\right)^2 + 2\Delta_3^2} \quad (10.5)$$

with the average valence band edge E_{v} and

$$\theta_{\epsilon} = D_3\epsilon_z + 2D_4\epsilon_t \quad (10.6)$$

$$\lambda_{\epsilon} = D_1\epsilon_z + 2D_2\epsilon_t. \quad (10.7)$$

As a result of the negative crystal-field split energy $\Delta_{\text{cr}} = -0.169$ eV in AlN, the light-hole band edge E_{lh} is above the heavy-hole band edge E_{hh} in all of our AlGaN layers. We therefore use the unstrained band edge E_{lh}^0 as reference in the calculation of the conduction band edge [9]

$$E_{\text{c}} = E_{\text{lh}}^0 + E_{\text{g}}^0 + P_{\text{ce}}, \quad (10.8)$$

with the hydrostatic energy shift

$$P_{c\epsilon} = a_{cz}\epsilon_z + 2a_{ct}\epsilon_t. \quad (10.9)$$

The hydrostatic deformation potential is anisotropic (a_z, a_t), and half of the deformation is assumed to affect the conduction band (a_{cz}, a_{ct}). For a given material, a_{cz} and a_{ct} can be translated into the isotropic APSYS input parameter

$$a_c = \frac{a_{ct} - a_{cz} \frac{C_{13}}{C_{33}}}{1 - \frac{C_{13}}{C_{33}}}. \quad (10.10)$$

The AlGa_xN band gap is known to deviate from the linear Vegard law and a wide range of bowing parameters C_g has been reported [7]. We adopt an average value of $C_g = 0.7$ eV and approximate the unstrained Al_xGa_{1-x}N band gap by

$$E_g^0(x) = xE_g^0(\text{AlN}) + (1-x)E_g^0(\text{GaN}) - x(1-x)C_g. \quad (10.11)$$

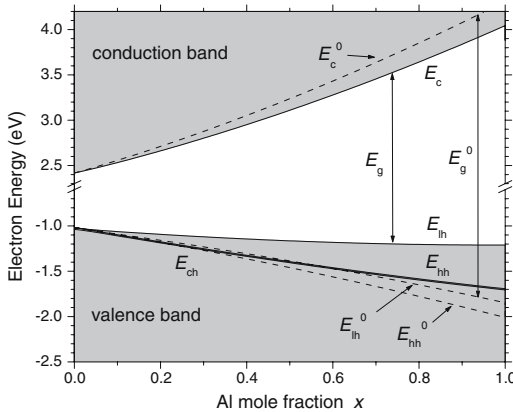


Fig. 10.2. Band edges of Al_xGa_{1-x}N grown on GaN (solid — strained, dashed — unstrained).

Figure 10.2 plots the Al_xGa_{1-x}N band edges with strain (solid lines) and without strain (dashed lines). For GaN, E_{hh} is the top valence band edge. For $x > 0.02$, E_{lh} becomes the top valence band edge, which increasingly reduces the effective band gap $E_g(x)$ compared with the unstrained band gap $E_g^0(x)$. E_{ch} is always slightly below E_{hh} . As $E_{lh}(x)$ varies little with

increasing x , the valence band offset between different AlGaIn layers is small, leading to poor hole confinement in the quantum wells. We here consider the valence band offset ratio $\Delta E_v/\Delta E_g = 0.3$ for unstrained material, using $E_v(x) = -0.3 E_g^0(x)$. However, this ratio is an uncertain parameter that corresponds to the 0.85 eV extracted from the literature as a most reliable result for the GaN/AlN valence band offset [7].

The dispersion $E_c(\mathbf{k})$ of the conduction band can be characterized by a parabolic band model with electron effective masses m_c^t and m_c^z perpendicular and parallel to the c -growth direction, respectively. The three valence bands are nonparabolic. Near the Γ point, the bulk hole effective masses can be approximated as

$$m_{\text{hh}}^z = -m_0(A_1 + A_3)^{-1} \quad (10.12)$$

$$m_{\text{hh}}^t = -m_0(A_2 + A_4)^{-1} \quad (10.13)$$

$$m_{\text{lh}}^z = -m_0 \left[A_1 + \left(\frac{E_{\text{lh}} - \lambda_\epsilon}{E_{\text{lh}} - E_{\text{ch}}} \right) A_3 \right]^{-1} \quad (10.14)$$

$$m_{\text{lh}}^t = -m_0 \left[A_2 + \left(\frac{E_{\text{lh}} - \lambda_\epsilon}{E_{\text{lh}} - E_{\text{ch}}} \right) A_4 \right]^{-1} \quad (10.15)$$

$$m_{\text{ch}}^z = -m_0 \left[A_1 + \left(\frac{E_{\text{ch}} - \lambda_\epsilon}{E_{\text{ch}} - E_{\text{lh}}} \right) A_3 \right]^{-1} \quad (10.16)$$

$$m_{\text{ch}}^t = -m_0 \left[A_2 + \left(\frac{E_{\text{ch}} - \lambda_\epsilon}{E_{\text{ch}} - E_{\text{lh}}} \right) A_4 \right]^{-1}, \quad (10.17)$$

using the hole effective mass parameters A_i given in Table 10.2. Details on the numerical calculation procedure for quantum well valence bands are given in [9].

10.3.2 Carrier Transport

APSYS employs the traditional drift-diffusion model for semiconductors. The current density of electrons \mathbf{j}_n and holes \mathbf{j}_p is caused by the electrostatic field \mathbf{F} (drift) and by the concentration gradient of electrons and holes, ∇n and ∇p , respectively,

$$\mathbf{j}_n = q\mu_n n \mathbf{F} + qD_n \nabla n \quad (10.18)$$

$$\mathbf{j}_p = q\mu_p p \mathbf{F} - qD_p \nabla p, \quad (10.19)$$

with the elementary charge q , the mobilities μ_n and μ_p , and the carrier densities n and p . The diffusion constants D_n and D_p are replaced by mobilities using the Einstein relation $D = \mu k_B T/q$ with the Boltzmann constant k_B and the temperature T . The electric field is affected by the charge distribution, which includes electrons n and holes p as wells as dopant ions (p_D, n_A) and

other fixed charges N_f (the latter are of special importance in GaN-based devices to account for built-in polarization). This relationship is described by the Poisson equation

$$\nabla \cdot (\varepsilon \varepsilon_0 \mathbf{F}) = q(p - n + p_D - n_A \pm N_f). \quad (10.20)$$

Changes in the local carrier concentration are accompanied by a spatial change in current flow $\nabla \mathbf{j}$ and/or by the generation G or recombination R of electron–hole pairs. This relation is expressed by the continuity equations

$$q \frac{\partial n}{\partial t} = \nabla \cdot \mathbf{j}_n - q(R - G) \quad (10.21)$$

$$q \frac{\partial p}{\partial t} = -\nabla \cdot \mathbf{j}_p - q(R - G). \quad (10.22)$$

Generation of electron-hole pairs by reabsorption of photons is not considered in our simulation. The relevant carrier recombination mechanisms in our device are spontaneous recombination and Shockley–Read–Hall (SRH) recombination. Spontaneous (radiative) recombination is discussed below. The defect-related nonradiative SRH recombination rate is given by

$$R_{\text{SRH}} = \frac{np - n_i^2}{\tau_p^{\text{SRH}} \left(n + N_c \exp \left[\frac{E_t - E_c}{k_B T} \right] \right) + \tau_n^{\text{SRH}} \left(p + N_v \exp \left[\frac{E_v - E_t}{k_B T} \right] \right)}, \quad (10.23)$$

and it is governed by the SRH lifetimes τ_n^{SRH} and τ_p^{SRH} ($N_{c,v}$ — density of states of conduction, valence band; E_t — mid-gap defect energy). SRH lifetimes are different for electrons and holes, but the SRH recombination rate is usually dominated by the minority carrier lifetime so that $\tau_{\text{nr}} = \tau_n^{\text{SRH}} = \tau_p^{\text{SRH}}$ is assumed in the following. The nonradiative carrier lifetime τ_{nr} is a crucial material parameter for GaN-based LEDs. In fact, the low output power of LEDs is often attributed to the high defect density and the correspondingly short nonradiative lifetime of carriers in AlGaIn and GaN epitaxial layers. Defect density and nonradiative lifetime depend on the substrate used and on the growth quality, and they are hard to predict. As SRH lifetime studies have not yet been performed on our example LEDs, we assume the uniform value of 1 ns in our simulations. The SRH lifetime in quantum wells is of particular importance, and it may be used as a fit parameter to find agreement with experimental LED characteristics [4].

Our model includes Fermi statistics and thermionic emission of carriers at hetero-interfaces [6]. The doping densities given in Table 10.1 represent actual densities of free carriers. Although the Si donor exhibits a low ionization energy, the Mg acceptor is known for its high activation energy so that the Mg density is significantly above the hole density. The hole mobility is hardly investigated for AlGaIn, and Table 10.1 lists empirical estimations. In contrast, significant attention has been paid to electron mobility modeling and we use

approximate values extracted from Monte-Carlo simulations [10]. However, the metal-semiconductor contact resistance contributes significantly to the device bias. Figure 10.3 compares the calculated current - voltage (IV) characteristics with the measurement. Without contact resistance, the calculated IV curve shows a steep turn-on at 3.6 V. Better agreement with the measurement can be obtained by adding an ohmic p-contact resistance of 20 Ω to the simulation. This results in a linear IV slope that slightly deviates from the superlinear experimental curve. The superlinearity is possibly caused by a Schottky-type contact, which is hard to model [6].

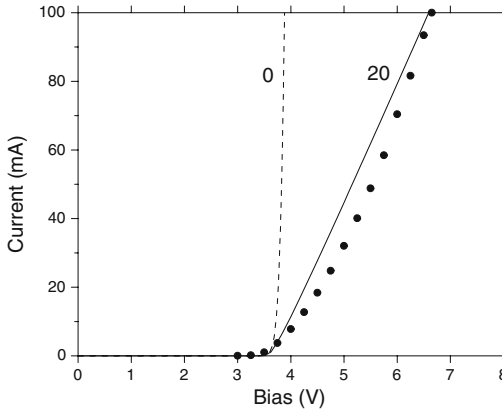


Fig. 10.3. Calculated current-voltage characteristics with (solid) and without (dashed) contact resistance (Ω); the dots give the measured curve [3].

Built-in polarization is another important issue for GaN LEDs. Spontaneous and piezoelectric polarization of nitride compounds is larger than in other III-V semiconductors. It depends on the compound's composition so that net charges remain at hetero-interfaces. Much theoretical effort has been invested in the prediction of these polarization charges, leading to relatively simple nonlinear interpolation formulas that are in close agreement with experimental observations [11]. For our $\text{Al}_x\text{Ga}_{1-x}\text{N}$ layers, the spontaneous polarization P_{sp} [C/m^2] is calculated as

$$P_{\text{sp}} = -0.09x - 0.034(1 - x) + 0.019x(1 - x). \quad (10.24)$$

The piezoelectric polarization P_{pz} [C/m^2] is given by

$$P_{\text{pz}} = x[-1.808\epsilon_t(x) - 7.888\epsilon_t^2(x)] + (1 - x)[-0.918\epsilon_t(x) + 9.541\epsilon_t(x)^2], \quad (10.25)$$

and it is linearly interpolated between the binary polarizations, which are nonlinear functions of the positive (tensile) transverse strain ϵ_t .³ Spontaneous and piezoelectric polarization add up to the surface charge density. At each interface, the difference of the surface charge densities gives the net polarization charge density, which is listed in Table 10.3 for all types of interfaces in our device. The $\text{Al}_{0.16}\text{Ga}_{0.84}\text{N}/\text{Al}_{0.20}\text{Ga}_{0.80}\text{N}$ superlattices are represented by a uniform $\text{Al}_{0.16}\text{Ga}_{0.84}\text{N}$ layer in our simulation as the internal SL interface charges compensate each other.

Table 10.3. Fixed Interface Charge Densities for Different Types of LED Interfaces.

Interface	Built-in Charge Density
$\text{GaN}/\text{Al}_{0.16}\text{Ga}_{0.84}\text{N}$	$+6.88 \times 10^{12} \text{cm}^{-2}$
$\text{Al}_{0.16}\text{Ga}_{0.84}\text{N}/\text{Al}_{0.10}\text{Ga}_{0.90}\text{N}$	$-2.73 \times 10^{12} \text{cm}^{-2}$
$\text{Al}_{0.10}\text{Ga}_{0.90}\text{N}/\text{Al}_{0.16}\text{Ga}_{0.84}\text{N}$	$+2.73 \times 10^{12} \text{cm}^{-2}$
$\text{Al}_{0.10}\text{Ga}_{0.90}\text{N}/\text{Al}_{0.30}\text{Ga}_{0.70}\text{N}$	$+9.89 \times 10^{12} \text{cm}^{-2}$
$\text{Al}_{0.30}\text{Ga}_{0.70}\text{N}/\text{Al}_{0.16}\text{Ga}_{0.84}\text{N}$	$-7.16 \times 10^{12} \text{cm}^{-2}$
$\text{Al}_{0.16}\text{Ga}_{0.84}\text{N}/\text{GaN}$	$-6.88 \times 10^{12} \text{cm}^{-2}$

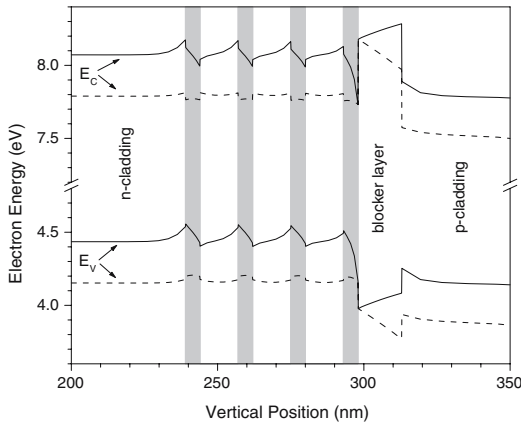


Fig. 10.4. Energy band diagram of the active region with (solid) and without (dashed) built-in polarization; the quantum wells are marked gray (E_c — conduction band edge, E_v — valence band edge).

³ The strain is compressive (negative) when AlN is used as substrate, resulting in a different formula (10.25) [11].

Figure 10.4 shows the energy band diagram of the MQW region with and without interface polarization charges. Built-in polarization causes a strong deformation of the quantum wells accompanied by a strong electrostatic field. Consequently, electrons and holes are separated within the wells and the spontaneous emission rate is reduced, limiting the LED output power. In addition, polarization affects the electron blocking by the $\text{Al}_{0.3}\text{Ga}_{0.7}\text{N}$ layer. Our comparison with measurements in the next section will show that (10.11) somewhat underestimates the band gaps in our device, in particular for the blocker layer. We therefore increase the band gap E_g^0 of $\text{Al}_{0.3}\text{Ga}_{0.7}\text{N}$ from 4.1 eV to 4.5 eV. This unstrained blocker band gap is reduced by strain to the actual band gap $E_g = 4.2$ eV (cf. Fig. 10.2).

10.3.3 Heat Generation and Dissipation

Self-heating often limits the performance of LEDs. Rising internal temperature reduces the band gap and leads to a red-shift of the emission wavelength. Device heating is generated when carriers transfer part of their energy to the crystal lattice. In our device, main heat sources are the electrical resistance, resulting in the Joule heat density

$$H_J = \frac{j_n^2}{q\mu_n n} + \frac{j_p^2}{q\mu_p p}, \quad (10.26)$$

and to a lesser extent, nonradiative carrier recombination, which gives the recombination heat density

$$H_R = R_{\text{SRH}} (E_{F_n} - E_{F_p}), \quad (10.27)$$

with the quasi-Fermi levels E_{F_n} and E_{F_p} for electrons and holes, respectively. The total heat power density $H_{\text{heat}}(x, y, z)$ enters the steady-state heat flux equation

$$-\nabla(\kappa_L \nabla T) = H_{\text{heat}}, \quad (10.28)$$

which is used to calculate the internal device temperature $T(x, y, z)$. The thermal conductivity κ_L is 130 W/Km for GaN and 285 W/Km for AlN. It is a strong function of composition for AlGaN due to alloy scattering [12]. The approximate numbers given in Table 10.1 also consider phonon mean free path restrictions by interface scattering [13].

Earlier investigations reveal a relatively low temperature slope near the active region of GaN devices due to the relatively high thermal conductivity [14]. Most of the temperature rise is caused by the thermal resistance of the sapphire substrate and the mounting, which are outside the simulated device region. We therefore add an empirical external resistance of 100 K/W to the heat sink at the bottom of our LED.

10.3.4 Spontaneous Photon Emission

The local spontaneous emission rate in bulk AlGaIn is approximated by

$$R_{\text{sp}} = B(np - n_i^2) \quad (10.29)$$

using the bimolecular recombination coefficient $B = 2 \times 10^{-10} \text{cm}^3/\text{s}$ (n_i - intrinsic density). This simple equation includes the full spectrum of photons generated by spontaneous band-to-band recombination processes. The spontaneous emission spectrum of our quantum wells is calculated as a function of the photon energy $h\nu$ by

$$r_{\text{sp}}(h\nu) = \left(\frac{q^2 \hbar}{2m_0^2 \varepsilon \varepsilon_0} \right) \left(\frac{1}{\hbar\nu} \right) D_{\text{opt}} D_r |M|^2 f_c (1 - f_v), \quad (10.30)$$

with Planck's constant h , the free electron mass m_0 , and the photon frequency ν . The photon emission rate is proportional to the density of photon states

$$D_{\text{opt}}(h\nu) = \frac{\varepsilon n_r}{\pi^2 \hbar^3 c^3} (h\nu)^2, \quad (10.31)$$

with the reduced Planck constant $\hbar = h/2\pi$ and the light velocity c . For quantum wells of thickness d_z , the reduced density of states in each subband is

$$D_r = \frac{m_r}{\pi \hbar^2 d_z}, \quad (10.32)$$

and all subbands are added up in (10.30).

The transition strength is given by $|M|^2$ (transition matrix element), and its computation is based on the $\mathbf{k} \cdot \mathbf{p}$ electron band structure model outlined in Sec. 10.3.1. $|M|^2$ is averaged over all photon polarization directions. For a quantum well grown in the hexagonal c direction, the transition matrix elements for heavy (hh), light (lh), and crystal-field holes (ch), respectively, are

$$|M_{\text{hh}}^{\text{TE}}|^2 = \frac{3}{2} O_{ij} (M_{\text{b}}^{\text{TE}})^2 \quad (10.33)$$

$$|M_{\text{lh}}^{\text{TE}}|^2 = \frac{3}{2} \cos^2(\theta_e) O_{ij} (M_{\text{b}}^{\text{TE}})^2 \quad (10.34)$$

$$|M_{\text{ch}}^{\text{TE}}|^2 = 0 \quad (10.35)$$

$$|M_{\text{hh}}^{\text{TM}}|^2 = 0 \quad (10.36)$$

$$|M_{\text{lh}}^{\text{TM}}|^2 = 3 \sin^2(\theta_e) O_{ij} (M_{\text{b}}^{\text{TM}})^2 \quad (10.37)$$

$$|M_{\text{ch}}^{\text{TM}}|^2 = 3 O_{ij} (M_{\text{b}}^{\text{TM}})^2. \quad (10.38)$$

These equations consider the angle θ_e of the electron \mathbf{k} vector with the k_z direction

$$k_z = |\mathbf{k}| \cos(\theta_e), \quad (10.39)$$

with $\cos(\theta_e) = 1$ at the Γ point of the quantum well subband. For transverse electric (TE) polarization, the photon electric field vector lies within the quantum well plane, whereas the photon magnetic field vector lies within the quantum well plane for transverse magnetic (TM) polarization. The matrix element also depends on the photon energy through the quantum well dispersion functions $E_m(\mathbf{k})$. It is different for each subband m . The overlap integral O_{ij} of the electron and hole wave functions can assume values between 0 and 1. At the Γ point, O_{ij} is nonzero only for subbands with the same quantum number m . Away from the Γ point, O_{ij} may be nonzero for any transition. Thus, at higher photon energies, summation over all possible subband combinations is included in the calculation. The anisotropic bulk momentum matrix elements are given by [15]

$$(M_b^{\text{TM}})^2 = \frac{m_0}{6} \left(\frac{m_0}{m_c^z} - 1 \right) \frac{(E_g + \Delta_1 + \Delta_2)(E_g + 2\Delta_2) - 2\Delta_3^2}{E_g + 2\Delta_2} \quad (10.40)$$

$$(M_b^{\text{TE}})^2 = \frac{m_0}{6} \left(\frac{m_0}{m_c^t} - 1 \right) \frac{E_g[(E_g + \Delta_1 + \Delta_2)(E_g + 2\Delta_2) - 2\Delta_3^2]}{(E_g + \Delta_1 + \Delta_2)(E_g + \Delta_2) - \Delta_3^2}. \quad (10.41)$$

Note that the bulk electron mass is different in transversal (m_c^t) and in parallel directions (m_c^z) relative to the hexagonal c axis. The material parameters are given in Table 10.2.

The Fermi factor $f_c(1 - f_v)$ in (10.30) gives the probability that the conduction band level is occupied and the valence band level is empty at the same time. The final spontaneous emission spectrum $r_{\text{spon}}(h\nu)$ is obtained by including the transition energy broadening according to

$$r_{\text{spon}}(h\nu) = \frac{1}{\pi} \int dE r_{\text{sp}}(E) \frac{\Gamma_s}{(h\nu - E)^2 + \Gamma_s^2} \quad (10.42)$$

using a Lorentzian line shape with the half-width $\Gamma_s = 6.6$ meV in our simulation.

10.3.5 Ray Tracing

Only a small fraction of generated photons is able to escape from the LED. This is attributed to total internal reflection as well as to internal absorption. Calculation of the external light power requires 3D ray tracing from every emission point within the device, weighted by the local emission rate. The ray tracing model is based on simple geometrical optics. Assuming equal numbers of TE and TM polarized photons, Fresnel's formulas are employed to account for reflection

$$r_{12}^{\text{TE}} = \frac{E_r^{\text{TE}}}{E_i^{\text{TE}}} = \frac{n_{r1} \cos \vartheta_i - n_{r2} \cos \vartheta_t}{n_{r1} \cos \vartheta_i + n_{r2} \cos \vartheta_t} \quad (10.43)$$

$$r_{12}^{\text{TM}} = \frac{E_r^{\text{TM}}}{E_i^{\text{TM}}} = \frac{n_{r2} \cos \vartheta_i - n_{r1} \cos \vartheta_t}{n_{r2} \cos \vartheta_i + n_{r1} \cos \vartheta_t} \quad (10.44)$$

and transmission

$$t_{12}^{\text{TE}} = \frac{E_t^{\text{TE}}}{E_i^{\text{TE}}} = \frac{2n_{r1} \cos \vartheta_i}{n_{r1} \cos \vartheta_i + n_{r2} \cos \vartheta_t} \quad (10.45)$$

$$t_{12}^{\text{TM}} = \frac{E_t^{\text{TM}}}{E_i^{\text{TM}}} = \frac{2n_{r1} \cos \vartheta_i}{n_{r2} \cos \vartheta_i + n_{r1} \cos \vartheta_t} \quad (10.46)$$

of the optical field at each light ray transition from material 1 to material 2 (E_i — incident field, E_r — reflected field, E_t — transmitted field, ϑ_i — incident angle, ϑ_t — angle of refraction as given by Snell's law). The multitude of reflections and the variety of possible light paths in our LED elongates the computation time. We therefore limit the number of initial rays to 6000.

Material parameters are the refractive index and the absorption coefficient, which are both a function of photon energy and alloy composition. We adopt a physics-based model developed by Adachi for photon energies close to the semiconductor band gap [16]. For nitride III–V compounds, the valence band splitting is very small and Adachi's model for the transparency region can be approximated by only one interband transition giving the refractive index

$$n_r^2(h\nu) = A \left(\frac{h\nu}{E_g} \right)^{-2} \left\{ 2 - \sqrt{1 + \left(\frac{h\nu}{E_g} \right)} - \sqrt{1 - \left(\frac{h\nu}{E_g} \right)} \right\} + B. \quad (10.47)$$

This approximation shows good agreement with measurements on GaN, AlN, and InN [17]. For $\text{Al}_x\text{Ga}_{1-x}\text{N}$ with $x < 0.38$, the material parameters

$$A(x) = 9.827 - 8.216x - 31.59x^2 \quad (10.48)$$

$$B(x) = 2.736 + 0.842x - 6.293x^2 \quad (10.49)$$

have been extracted from measurements [18]. The resulting data for our device are listed in Table 10.1. For 340-nm wavelength, the photon energy is larger than the GaN band gap and the overall absorption in our LED is dominated by the GaN layers with an absorption coefficient of $\alpha = 11 \times 10^4 \text{ cm}^{-1}$. The ray tracing also considers the semi-transparent p-contact, which comprises a 3-nm-thick palladium layer ($n_r = 1.1, \alpha = 18 \times 10^4 \text{ cm}^{-1}$) and a 5-nm-thick gold layer ($n_r = 1.4, \alpha = 59 \times 10^4 \text{ cm}^{-1}$). Background loss of $\alpha = 20 \text{ cm}^{-1}$ is assumed for all other layers.

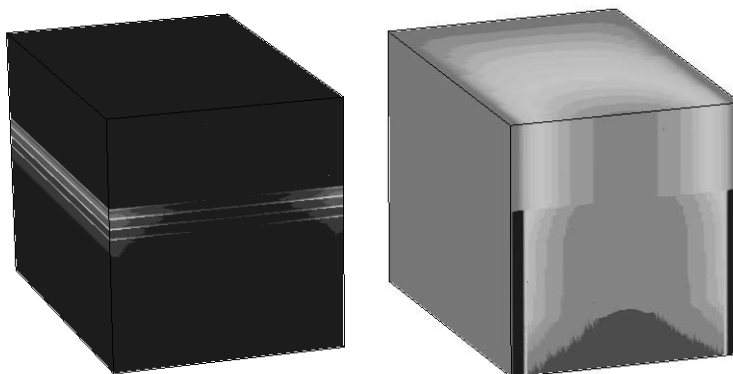


Fig. 10.5. 3D plots of the LED giving the radiative recombination rate on the left and the vertical current density on the right at 100-mA injection current (the discontinuity near the MQW is related to strong lateral current).

10.4 Results and Discussion

10.4.1 Internal Device Analysis

Figure 10.5 shows on the left a 3D plot of the LED radiative recombination rate, which is strongest in the four quantum wells and which decays toward the device center, in agreement with experimental observations. This lateral nonuniformity is attributed to current crowding along the sides with an adjacent n-contact (right-hand side of Fig. 10.5). The current density is highest in the two corners of the U-shaped contact. This corner position is therefore chosen in the next few graphs to show vertical profiles of different physical properties, all at 100-mA injection current.

Figure 10.6 plots the vertical profile of electron and hole density. As a result of the quantum well deformation by the polarization charges shown in Fig. 10.4, the hole density peaks on the *n*-side of each well and the electron density on the *p*-side. This separation of electron and hole wavefunctions reduces the radiative emission rate. The quantum well electron density is higher than the hole density, and it is highest in the *p*-side asymmetric quantum well because of the better electron confinement. The highest hole density occurs above the electron blocker layer due to the valence band edge maximum caused by the negative interface charges. Figure 10.7 shows vertical profiles of the electron-hole recombination rates. The nonradiative Shockley–Read–Hall recombination peaks within the quantum wells. It is about two orders of magnitude stronger than the radiative recombination. In other words, not more than 1% of the injected carriers contribute to the light emission. Figure 10.7 also indicates significant carrier leakage from the quantum wells, which leads to additional carrier recombination outside the wells. Non-radiative recomb-

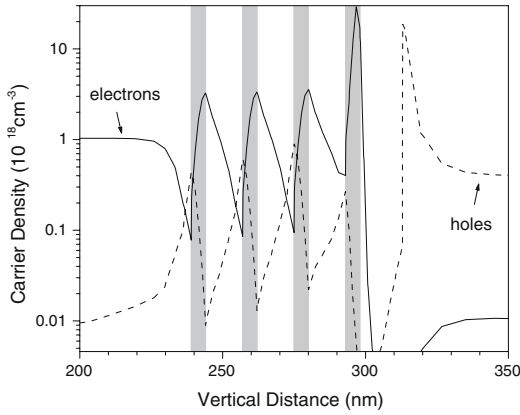


Fig. 10.6. Vertical profile of electron and hole density

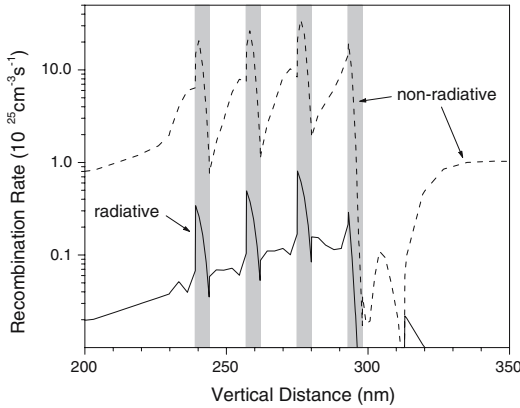


Fig. 10.7. Vertical profile of radiative and nonradiative recombination rate.

nation occurs even beyond the electron blocker layer, where leaking electrons meet injected holes.

Vertical components of the current density are plotted in Fig. 10.8 (the current is negative because it flows from the top to the bottom). Ideally, electrons and holes meet in the quantum wells and recombine completely. However, some holes leave the MQW region and leak into the lower n-cladding where they recombine with electrons. More severe is the electron leakage in the opposite direction. A large part of the electrons injected from the n-side

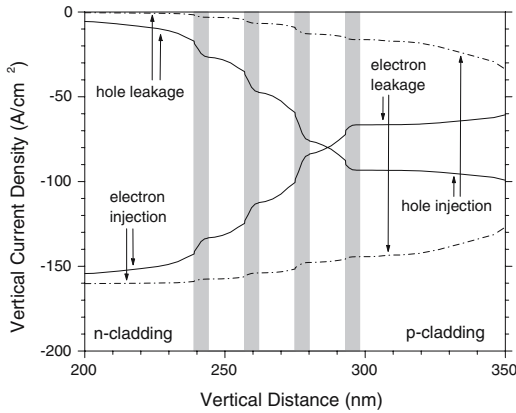


Fig. 10.8. Vertical current density j_y of electrons and holes (dashed — original blocker band gap, solid — adjusted blocker band gap).

into the MQW leaks into the p-cladding layer. This electron leakage strongly depends on the conduction band offset between the top quantum well and the blocker layer (cf. Fig. 10.4). According to our default material parameters from [7], the offset is 153 meV, resulting in very strong electron leakage and in light emission below the measured light power (dashed lines). Considering the large variation of band gap and offset data extracted from the literature [7], we therefore use it as fit parameter to find better agreement with the measured light output. The fit of the light-current characteristic below is obtained using a 403-meV conduction band offset between quantum well and blocker layer (solid lines in Fig. 10.8).

10.4.2 External Device Characteristics

The calculated emission spectrum is compared with the measurement in Fig. 10.9. The theoretical spectrum exhibits multiple peaks and shoulders attributed to different transition energies within the quantum wells. Without the electrostatic field, the asymmetric top well exhibits a lower emission energy than the other three symmetric quantum wells. The built-in polarization field leads to a shift of the existing quantum levels and to the creation of additional levels, especially in the top quantum well. However, the measured spectrum is smoother, probably due to statistical variations of the quantum well structure. There may be less polarization charges in the real device, or the shape of the quantum well may deviate otherwise from the theoretical assumption. The experimental emission peak is at slightly higher photon energy than the calculated one, which may also be attributed to nonideal

quantum well growth or to an overestimation of the band gap by (10.11). The experimental peak hardly shifts with increasing current, indicating little self-heating. In our simulation, the internal temperature rise of up to 63 K leads to a slight shift of the emission peak by about 1 nm. Thus, the assumed thermal resistance of 100 K/W seems to slightly overestimate the influence of substrate and heat sinking on our LED self-heating. The temperature difference within the simulation region is less than 1 K due to the relatively high thermal conductivity of nitride alloys.

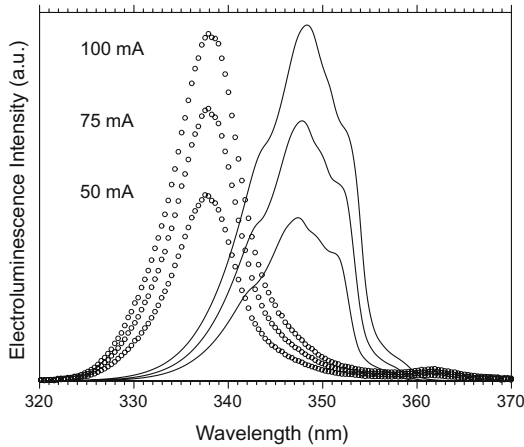


Fig. 10.9. LED emission spectra at three different injection currents (dots — measurement [3], lines — simulation).

Most photons are unable to escape from the LED, due to total internal reflection, mainly at the device surfaces, and to photon absorption, primarily in the bottom GaN layer. The detected external quantum efficiency η_{det} gives the ratio of detected photons to the injected electron-hole pairs. It is calculated from

$$\eta_{\text{det}} = \eta_{\text{int}} \eta_{\text{opt}} \eta_{\text{cap}} , \quad (10.50)$$

with the internal quantum efficiency η_{int} (fraction of photons generated inside the LED per electron-hole pair injected), the photon extraction efficiency η_{opt} (fraction of escaped photons per photon generated inside the LED), and the detector capture efficiency η_{cap} (fraction of detected photons per escaped photons). The last number cannot be exactly determined in this study. A large-area detector (100 mm²) was used to measure the top emission, and we estimate $\eta_{\text{cap}} = 82\%$. The strong absorption in GaN prevents any bottom emission. Only $\eta_{\text{opt}} = 4.5\%$ of all internally generated photons escape from the LED. About 78% of all photons are absorbed within the GaN layers and the remaining 17% are absorbed by the semi-transparent Pd/Au contact.

But the main limitation of the emitted light power originates from the internal quantum efficiency, which is $\eta_{\text{int}} = 0.96\%$ for 100-mA injection current. As indicated by the strong nonradiative recombination in Fig. 10.7, less than 1 out of 100 injected electron-hole pairs generate a photon within the quantum wells. Nonradiative recombination and carrier leakage are key causes for the low external quantum efficiency of $\eta_{\text{det}} = 0.035\%$, which is close to the measured value of 0.032% [3].

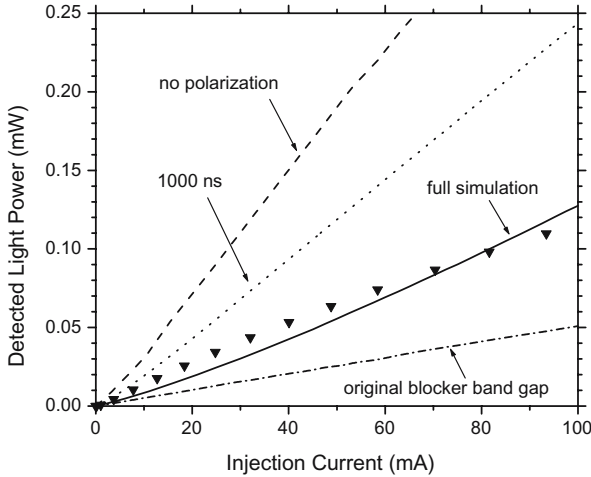


Fig. 10.10. LED emission light vs. current characteristics (triangles — measurement [3], lines — simulation).

Figure 10.10 plots the detected light power as a function of injection current (LI characteristic). The simulation is in good agreement with the measurement, which indicates that model and parameters are fairly accurate in our simulation. The solid line in Fig. 10.10 is fitted to the measurement by increasing the blocker layer band gap from $E_g^0 = 4.1$ eV to 4.5 eV. For comparison, Fig. 10.10 also shows the much lower output power calculated with the original blocker band gap, which is attributed to stronger carrier leakage (cf. Fig. 10.8). Without built-in polarization, electrons and holes are less separated within each quantum well and the radiative emission rate is significantly enhanced, as shown by the dashed curve in Fig. 10.10 ($\eta_{\text{int}} = 2.9\%$). Finally, the dotted curve represents a simulation with extremely long carrier lifetime of $\tau_{\text{nr}} = 1000$ ns within the quantum wells. Due to the suppressed nonradiative recombination in the wells, the internal quantum efficiency is doubled to $\eta_{\text{int}} = 1.8\%$. This surprisingly low improvement underlines the detrimental effect of carrier leakage from the MQW; i.e., more than 98% of all carriers recombine outside the quantum wells.

10.5 Summary

We have presented a self-consistent three-dimensional simulation of electronic, optical, and thermal processes in AlGaIn/GaN ultraviolet light-emitting diodes. Good agreement with measurements is achieved underlining the accuracy of models and parameters. We find that the low output power of practical devices is mainly restricted by the low internal quantum efficiency of less than 1%, which is primarily attributed to carrier leakage from the quantum wells.

Acknowledgment

This work was partially supported by the Solid-State Lighting and Display Center (Director: Prof. Shuji Nakamura) at the University of California at Santa Barbara. J. P. is grateful to Dr. Thomas Katona and Dr. Stacia Keller for valuable discussions and measurements. S. L. acknowledges Dr. Oleksiy Shmatov's contribution to the initial phase of the 3D ray-tracing project.

References

1. E. F. Schubert: *Light-Emitting Diodes* (Cambridge Univ. Press, Cambridge 2003)
2. S. Nakamura: Development and future prospects of GaN-based LEDs and LDs. In: *Introduction to Nitride Semiconductor Blue Lasers and Light-Emitting Diodes*, ed by S. Nakamura and S. F. Chichibu (Taylor & Francis, London 2000)
3. T. Katona: Development of Ultraviolet Nitride-based Light-Emitting Diodes. PhD Thesis, University of California, Santa Barbara (2003)
4. J. Piprek, T. Katona, S. P. DenBaars, and S. Li: 3D Simulation and Analysis of AlGaIn/GaN Ultraviolet Light-Emitting Diodes. In: *Light-Emitting Diodes: Research, Manufacturing and Applications VIII* SPIE Proceedings **5366** (The International Society for Optical Engineering, Bellingham 2004)
5. APSYS Version 2003.12.01 by Crosslight Software, Inc., Burnaby, Canada (<http://www.crosslight.com>)
6. J. Piprek: *Semiconductor Optoelectronic Devices: Introduction to Physics and Simulation* (Academic Press, San Diego 2003)
7. I. Vurgaftman and J. R. Meyer: *J. Appl. Phys.* **94**, 3675 (2003)
8. S. L. Chuang and C. S. Chang: *Phys. Rev. B* **54**, 2491 (1996)
9. S. L. Chuang and C. S. Chang: *Semicond. Sci. Technol.* **12**, 252 (1997)
10. M. Farahmand, C. Garetto, E. Bellotti, K. F. Brennan, M. Goano, E. Ghillino, G. Ghione, J. D. Albrecht, and P. P. Ruden: *J. Appl. Phys.* **48**, 535 (2001)
11. V. Fiorentini, F. Bernardini, and O. Ambacher: *Appl. Phys. Lett.* **80**, 1204 (2002)
12. B. C. Daly, H. J. Maris, A. V. Nurmikko, M. Kuball, and J. Han: *J. Appl. Phys.* **92**, 3820 (2002)

13. J. Piprek, T. Troger, B. Schroter, J. Kolodzey, and C. S. Ih: IEEE Photon. Technol. Lett. **10**, 81 (1998)
14. J. Piprek and S. Nakamura: IEE Proceedings, Optoelectronics **149**, 145 (2002)
15. S. L. Chuang: IEEE J. Quantum Electron. **32**, 1791 (1996)
16. S. Adachi: *Physical Properties of III-V Semiconductor Compounds* (Wiley, New York 1992)
17. T. Peng and J. Piprek: Electron. Lett. **32**, 2285 (1996)
18. G. M. Laws, E. C. Larkins, I. Harrison, C. Molloy, and D. Somerford: J. Appl. Phys. **89**, 1108 (2001)